mater.scichina.com link.springer.com

Sci China Mater 2025, 68(8): 2725–2734
https://doi.org/10.1007/s40843-025-3458-1

Enhanced photoluminescence quantum yield in metal halide perovskites *via* trace Ag doping

Machao Wang[1,2†], Yangmin Tang[1,2†], Guiqiang Pu[3], Chengbin Kang[4], Zhiqiang Wang[5], Lijia Liu[5], Jing Li[6], Zhenzhen Zhou[1], Wei Chen[7], Dong Wang[1,2*] and Jiacheng Wang[1,3*]

ABSTRACT **Self-trapped excitons are prevalent in metal halide perovskites (MHPs) characterized by soft lattices and strong exciton-phonon coupling, emitting photons with broadband emission and large Stokes shifts, rendering them particularly well-suited for applications in light-emitting diodes. But their photoluminescence quantum yields (PLQY) are limited by both high exciton binding energy and halogen-vacancy-associated non-radiative recombination. Here, we show that PLQY could be enhanced by a factor of 5.6 from 16% to 89% through doping trace Ag into $Cs_2NaBiCl_6$ double perovskites, superior to those of previous $Cs_2NaBiCl_6$-based emitters. Experimental and theoretical studies reveal that trace Ag-initiated covalent interactions could reduce the exciton binding energy by 0.12 eV due to local symmetry breaking, thus improving the photoexcitation process. Also, this covalent interaction could passivate Cl vacancy defects, suppressing non-radiative recombination. Therefore, $Cs_2NaBiCl_6$: 0.7% Ag^+ could accumulate active self-trapped excitons to obtain high PLQY. Assembly of near-infrared light-emitting diodes using $Cs_2NaBiCl_6$: 0.7% Ag^+ illustrates their valuable applications in nondestructive spectral analysis and night vision illumination. This work shows an effective strategy of improving photoemission of MHPs with high PLQY for advanced optoelectronic applications.**

Keywords: Ag doping, photoluminescence quantum yields, local symmetry breaking, defect passivation, self-trapped excitons

INTRODUCTION

Self-trapped excitons (STEs) have the property of broadband emission, which has attracted much attention in the fields of illumination, night vision, and non-destructive analysis [1–4]. For lead-free metal halide perovskites (LFMHPs), which possess soft lattice and strong exciton-phonon coupling characteristics, soft lattice distortions would facilitate STEs generation [5]. Unfortunately, the potential applications of LFMHPs are limited by their low intrinsic emission (photoluminescence quantum yield, PLQY<15%) [6]. To obtain single-component broadband emission materials with enhanced PLQY, the perovskite systems with ns^2 ions (Sb^{3+}, Sn^{2+}, Bi^{3+}) have also attracted great interest [7]. Doping ns^2 ions in perovskites can obtain intense broadband emission due to the strong optical absorption of ns^2 ions in the ultraviolet region ($s^2 \rightarrow sp$ transition, parity allowed) [8,9]. Nevertheless, given the strong dependence between the stereochemical effects of lone electron pairs within ns^2 ions and the metal-ligand coordination environment, a proper host lattice is essential for this type of perovskite. For example, Sb^{3+} doping into Cs_2ZnCl_4 perovskite resulted in a high PLQY of 70% (emission peak at 745 nm) [10]. However, the defects induced by lattice distortion after ns^2 ions doping limit the further enhancement of PLQY. Therefore, the comprehensive material design strategies are needed to passivate the material defect states and further increase the STEs density.

As we know, both ionic and covalent bonds are intramolecular strong bonds in molecular solids, e.g., LFMHPs. The ionic bond is the electrostatic force that exists between oppositely charged ions, whereas the covalent bond is the sharing of an electron pair between two atoms [11]. In sharp contrast, the halogen ions in LFMHPs can easily form covalent bonds with some metal ions (e.g., Ag–Cl) in substitution for ionic bonds, favorable for optimizing coordination environments and suppressing halogen vacancies. In $Cs_2(Ag/Na)InCl_6$ double perovskites (DPs), the Ag/Na alloying favors the Jahn-Teller distortion and also leads to the formation of STEs [12]. However, in the $Cs_2(Ag/Na)BiCl_6$ system, the optimum PLQY value is only 51% [13]. This is due to the fact that the Ag/Na alloying strategy is based on local symmetry breaking, neglecting the positive effect of defect passivation on STEs.

Herein, we present that the PLQY of $Cs_2NaBiCl_6$ (CNBC) DPs

[1] State Key Laboratory of High-Performance Ceramics and Superfine Microstructure, Shanghai Institute of Ceramics, Chinese Academy of Sciences, Shanghai 200050, China
[2] Center of Materials Science and Optoelectronics Engineering, University of Chinese Academy of Sciences, Beijing 100049, China
[3] Zhejiang Provincial Key Laboratory for Island Green Energy and New Materials, Institute of Electrochemistry, School of Materials Science and Engineering, Taizhou University, Taizhou 318000, China
[4] Department of Applied Physics, The Hong Kong Polytechnic University, Hong Kong 999077, China
[5] Department of Chemistry, Western University, London, ON N6A5B7, Canada
[6] Key Laboratory of Photochemical Conversion and Optoelectronic Materials, Technical Institute of Physics and Chemistry, Chinese Academy of Sciences, Beijing 100190, China
[7] Department of Materials Design and Innovation, University at Buffalo, The State University of New York, Buffalo, NY 14260, USA
† Equally contributed to this work.
* Corresponding author (email: jiacheng.wang@tzc.edu.cn; wangd@mail.sic.ac.cn)

with soft lattices could be significantly enhanced by 5.6 times through trace Ag-induced strong Ag–Cl covalent bonds, obtaining efficient broadband emission (Fig. 1). The as-formed CNBC: Ag^+ with only 0.7% Ag doping shows a high PLQY of 89%, which can be attributed to defect passivation in the soft lattice and symmetry breaking. The 18-electron Ag^+ is more ionically polarized towards Cl^- than the 8-electron Na^+ in CNBC, so enhanced covalency could be realized after trace Ag doping. The theoretical calculation combined with X-ray absorption fine structure characterization (XAFS) confirms the introduction of Ag–Cl covalent bonds into CNBC, thus leading to local symmetry breaking and Cl vacancy suppression in CNBC: Ag^+. Local symmetry breaking could promote the exciton dissociation process, enabling enhanced optical absorption of Bi^{3+} in the UV region ($s^2 \rightarrow sp$ transition, parity allowed) [13–16]. Meanwhile, the passivation of Cl vacancies could promote the radiative recombination of STEs. After introducing trace Ag, the emission peak of CNBC: 0.7% Ag^+ was still located at 680 nm, unlike that at 620 nm for $Cs_2AgBiCl_6$ (CABC). This study provides a covalency-modulation strategy by doping trace metals in ionic-bonds-enriched LFMHPs to improve PLQY and stability.

EXPERIMENTAL SECTION

Materials preparation

The double perovskite solution was prepared by dissolving CsCl (Aladdin, 99.999%), NaCl (Adamas, 99.99%), AgCl (Aladdin, 99.5%), and $BiCl_3$ (Adamas, 99.0%) with a molar ratio of 2:(1 −x):x:1 in hydrochloric acid (12 M) in air at room temperature. Then, 20 mL of this solution (0.1 M) was transferred to a 50 mL Teflon-lined hydrothermal kettle and placed in an oven at 180 °C for 12 h. The kettle was cooled to 60 °C at a controlled cooling rate of 5 °C per hour. The resulting crystals were filtered and washed with anhydrous ethanol, followed by drying at 60 °C for 12 h. The x-values are 0.01, 0.02, 0.04 and 0.06 corresponding to Ag molar concentrations of 0.003, 0.007, 0.008 and 0.012 in final CNBC: Ag^+, respectively.

Materials characterization

Powder X-ray diffraction data were collected by the detector Rigaku, D/max 2550V with Cu-$K_{\alpha 1}$ radiation (λ = 0.154187 nm).

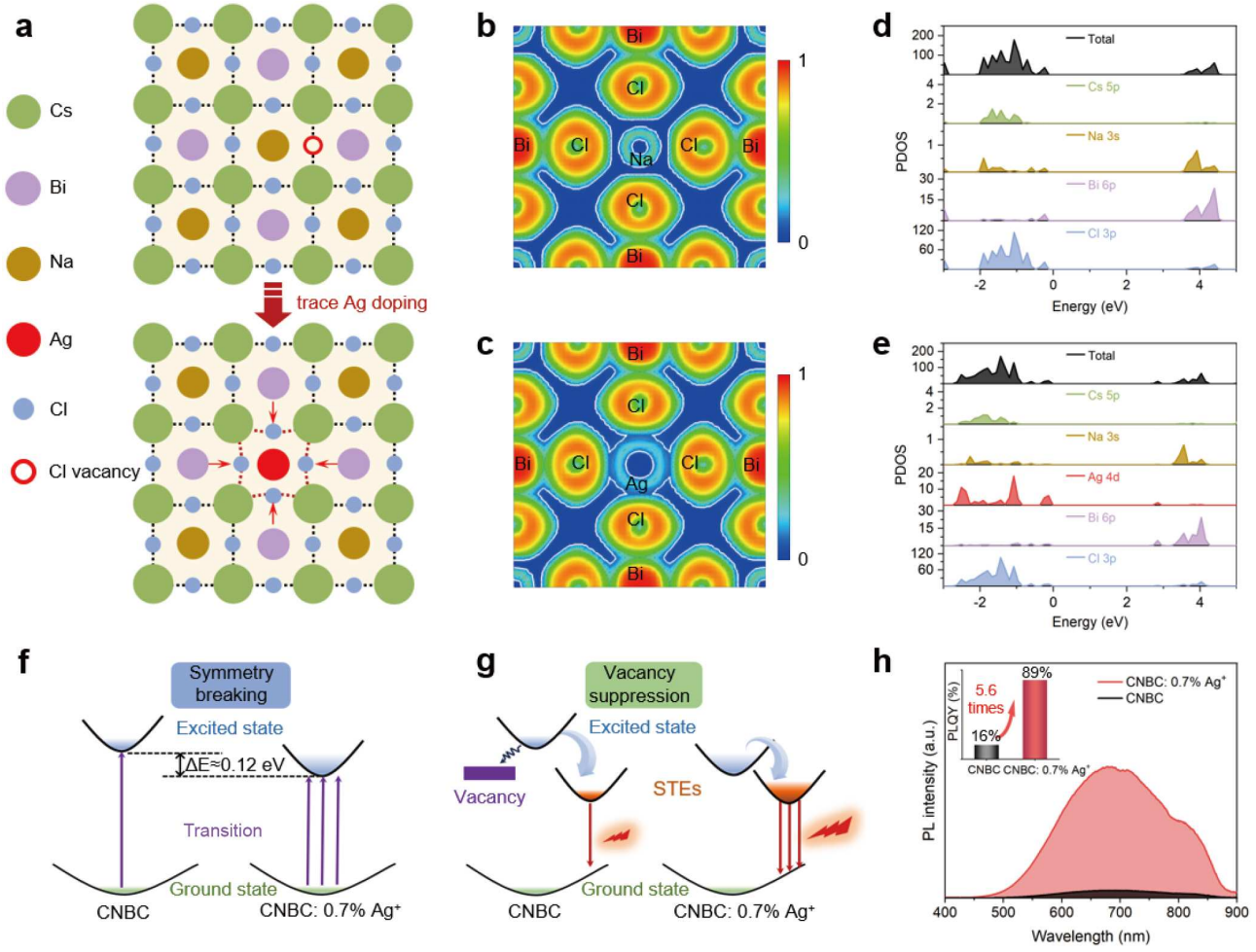

Figure 1 Design concept of trace Ag doping into CNBC for broadband emission enhancement. (a) Schematic illustration of the introduction of trace Ag into CNBC, resulting in local symmetry breaking and efficient vacancy suppression. The electron localization functions of CNBC (b) and CNBC: Ag^+ (c). The calculated band structures of CNBC (d) and CNBC: Ag^+ (e). (f) Schematic of the photophysical process for symmetry-breaking-induced carrier generation. (g) Schematic of the photophysical process for vacancy suppression to enhance the STEs. (h) Photoluminescence spectra under excitation of 350 nm for CNBC and CNBC: 0.7% Ag^+ measured at 25 °C. The inset shows the corresponding PLQY of CNBC and CNBC: 0.7% Ag^+.

ICP-OES measurements were performed at inductively coupled plasma atomic emission spectroscopy (Horiba Ultima Expert, Agilent ICPOES730). Raman spectra were recorded with an excitation laser source of 532 nm (HORIBA HR Evolution). TEM and SEM images were obtained by using TEM (JEOL JEM-2100F) and SEM (JEOL JSM-7800F). The XPS spectra were measured by using a Shimadzu AXIS ULTRA DLD spectrometer using a monochromatic Al Kα source (12 kV, 10 mA). The absorbance spectra were obtained by a spectrophotometer (Shimadzu, UV-2600), using $BaSO_4$ as a reference sample. Photoluminescence and excitation spectra of $Cs_2NaBiCl_6$: Ag^+ DPs were measured using a Hitachi F4600 spectrofluorometer. Photoluminescence quantum yields were detected using a spectrofluorometer (Hamamatsu Photonics, Quantaurus QY Plus C13534-12). A regenerative-amplified Ti: sapphire laser system (Coherent) was used for Fs-TA spectroscopy measurements. The regenerative-amplified Ti: sapphire laser system (Legend Elite-1K-HE, 800 nm, 25 fs, 4 mJ/pulse, and 1 kHz repetition rate) was seeded with a mode-locked Ti: sapphire laser system (Vitara) and pumped with a Nd: YLF laser (Evolution 30). The main part of the output light of the regenerative-amplified Ti: sapphire laser was introduced into the optical parametric amplifiers (TOPAS-C) with the wavelength-tunable laser pulse from 290 nm to 2.6 μm. The pump beam with wavelength of 310 nm was used in the Fs-TA measurement. Luminescence lifetime and temperature-dependent PL emission spectra were tested with an Edinburgh FLS980 fluorescence spectrometer. The Bruker A300 instrument was used to measure the electron paramagnetic resonance. The Thermogravimetric data were collected under N_2 atmosphere (PerkinElmer Instruments, Diamond TG/DSC6300). The XAFS spectra at the Ag K- and Bi L_3-edge were acquired at the HXMA beamline at the Canadian Light Source. All spectra were measured in fluorescence mode and normalized to the incident photon flux. The data processing was conducted using the Demeter software package [17]. The fitting at the EXAFS region was only performed within the first shell (e.g., Ag–Cl and Bi–Cl). The *R*-space signal was obtained by a k^3-weighted Fourier transfer of EXAFS signal $\chi(k)$ over a *k*-range of 3.0 to 12.0 $Å^{-1}$ for Bi and of 3.0 to 9.1 $Å^{-1}$ for Ag. The fitting was performed in the *R*-space within a range between 1.0 and 3.0 Å. The amplitude reduction factor was set to be 0.8.

NIR LED assembly

The NIR LED was packed by combining the perovskite phosphors with a commercial 365 nm UV chip (San'an Optoelectronics Co., Ltd., 1 W, 365 nm). The phosphor and the UV curable adhesive were fully mixed in a 1:1 mass ratio and then uniformly coated on the UV Chip. The device was further cured at 80 °C for 8 h.

Device characterization

The luminescence spectrum of the device was obtained by an OHSP-350M LED Fast-Scan Spectrophotometer (Hangzhou Hopoo Light&Color Technology Co., Ltd.). The absorption spectral data of fruits were recorded by a fiber-optic spectrometer (NOVA highly sensitive spectrometer, ideaoptics).

DFT calculations

First principles calculations were performed by the Vienna *ab initio* simulation package (VASP) using density functional theory in Perdew-Burke-Ernzerhof generalized gradient approximation for the exchange correlation functional. $Cs_2NaBiCl_6$ was modeled with 40 atoms on the basis of the unit cell, and Ag ions doped $Cs_2NaBiCl_6$:Ag^+ were modeled according to the above $Cs_2NaBiCl_6$ model with a Na atom substituted by an Ag atom. First, the geometry optimizations were performed until the total energies and the Hellmann-Feynman forces on the atoms converged to 1×10^{-6} eV and 0.02 eV/Å, respectively. Both band structures and density of states were calculated using optimized lattice structures. The plane wave cutoff energy of 450 eV was used throughout the calculation. The k-point meshes for Brillouin zone sampling were 2×2×2 according to the Monkhorst-Pack scheme.

RESULTS AND DISCUSSION

Design concept of trace Ag doping into CNBC for broadband emission enhancement

CNBC shows a double perovskite 3D structure, in which each Bi^{3+} and Na^+ ions are coordinated with six Cl^- ions to form $[BiCl_6]^{3-}$ and $[NaCl_6]^{5-}$ units (Fig. 1a). These $[BiCl_6]^{3-}$ and $[NaCl_6]^{5-}$ octahedrons are stacked alternatively with Cs^+ ions occupying the gaps between the octahedrons. Both Ag^+ and Na^+ ions have similar ionic radii (1.29 Å for Ag^+, 1.16 Å for Na^+) [18]. Therefore, Ag^+ could be easily dissolved in CNBC and occupy the lattice sites of Na^+, leading to low lattice mismatch.

Then, density functional theory (DFT) calculations confirm that trace Ag-induced covalency (Ag–Cl) was successfully introduced into CNBC: Ag^+ based on the distribution of charge densities between atoms (Fig. 1b, c). In the case of Na–Cl, the bond charge densities at the nuclei of Na and Cl were different and dense, whereas for Ag–Cl, we observed a uniform distribution of charge densities between these atoms. It shows the covalent nature of Ag–Cl bonds. It is noteworthy that ion polarization was responsible for the nature of the chemical bonding between the surrounding chloride atoms and the monovalent ions in the lattice. Such different electron localization functions could inevitably affect the bond lengths of Bi–Cl (Supplementary Information, Fig. S1). Specifically, the bond length of Bi–Cl was increased from 2.725 Å (Bi–Cl–Na) to 2.744 Å (Bi–Cl–Ag) after Ag occupied the Na site. Therefore, the local site symmetry of Bi^{3+} would be broken, which could lead to an improvement in optical absorption [19]. Furthermore, we calculated the electronic structure and projected density of states of CNBC and CNBC: Ag^+ (Fig. 1d, e; Supplementary Information, Fig. S2). The calculated indirect band gap of CNBC was 3.72 eV, and the valence band (VB) maximum was mainly contributed by the Cl 3*p* orbital, while the conduction band (CB) minimum was primarily ascribed to the contribution of the Bi 6*p* and Cl 3*p* orbitals. CNBC: Ag^+ showed a smaller indirect band gap of 2.14 eV because of the contribution of Ag 4*d* and Cl 3*p* orbitals to the VB maximum. These results provide theoretical evidence of enhancing the covalency of CNBC by trace Ag doping.

The introduction of trace Ag–Cl covalent bonds into CNBC could produce two effects, symmetry breaking and vacancy suppression (Fig. 1a, f, g). This could promote the carrier generation and the STEs density. As shown in Fig. 1f, Ag–Cl covalency induces lattice shrinkage and breaks the $[BiCl_6]^{3-}$ octahedral symmetry of the Ag^+ neighboring sites, thus facilitating the $s^2 \rightarrow sp$ parity-allowed transition of Bi^{3+}. In detail, the

exciton binding energy could be lowered by 0.12 eV, in line with the trend of decreasing the forbidden band width. The low binding energy would promote the dissociation of excitons to form carriers, which then transfer to the self-trapped state for the subsequent STEs emission process [20]. On the other hand, the Cl vacancy was the nonradiative recombination center of electrons and holes [21], and this would hinder the transfer of carriers to the self-trapped state. The covalent interaction could suppress the chlorine vacancies well and reduce the rate of nonradiative recombination (Fig. 1g). In conclusion, symmetry breaking could promote carrier generation, and vacancy suppression could facilitate the carriers to form STEs. And both synergistically increase the STEs density. Thus, the PL intensity of the resulting CNBC: 0.7% Ag^+ crystals could be enhanced with the PLQY of 89%, which was 5.6 times higher than that of CNBC crystals (Fig. 1h).

Structure and chemical environments of trace Ag-doped CNBC: Ag^+

We then investigated the structure and chemical environments of CNBC: Ag^+ DPs. These Ag-doped CNBC DPs could be synthesized by solvothermal treatment of CsCl, NaCl, AgCl, and $BiCl_3$ in HCl (12 M) solution. The Ag^+ doping ratio in the final CNBC: Ag^+ samples was determined by inductively coupled plasma optical emission spectroscopy (ICP-OES). And the results show low Ag doping concentration (<2 mol%) in all samples (Table S1). The DPs with Ag^+ doping all exhibit the same X-ray diffraction (XRD) pattern as CNBC (space group: $Fm\bar{3}m$), indicating pure phase structures (Fig. 2a) [22–24]. The diffraction peak (220) was gradually shifted to a larger angle and approached CABC, showing a gradual lattice shrinkage due to the introduction of the covalent Ag–Cl bonds (2.768 Å) being shorter than the ionic Na–Cl bonds (2.805 Å). Under 532 nm

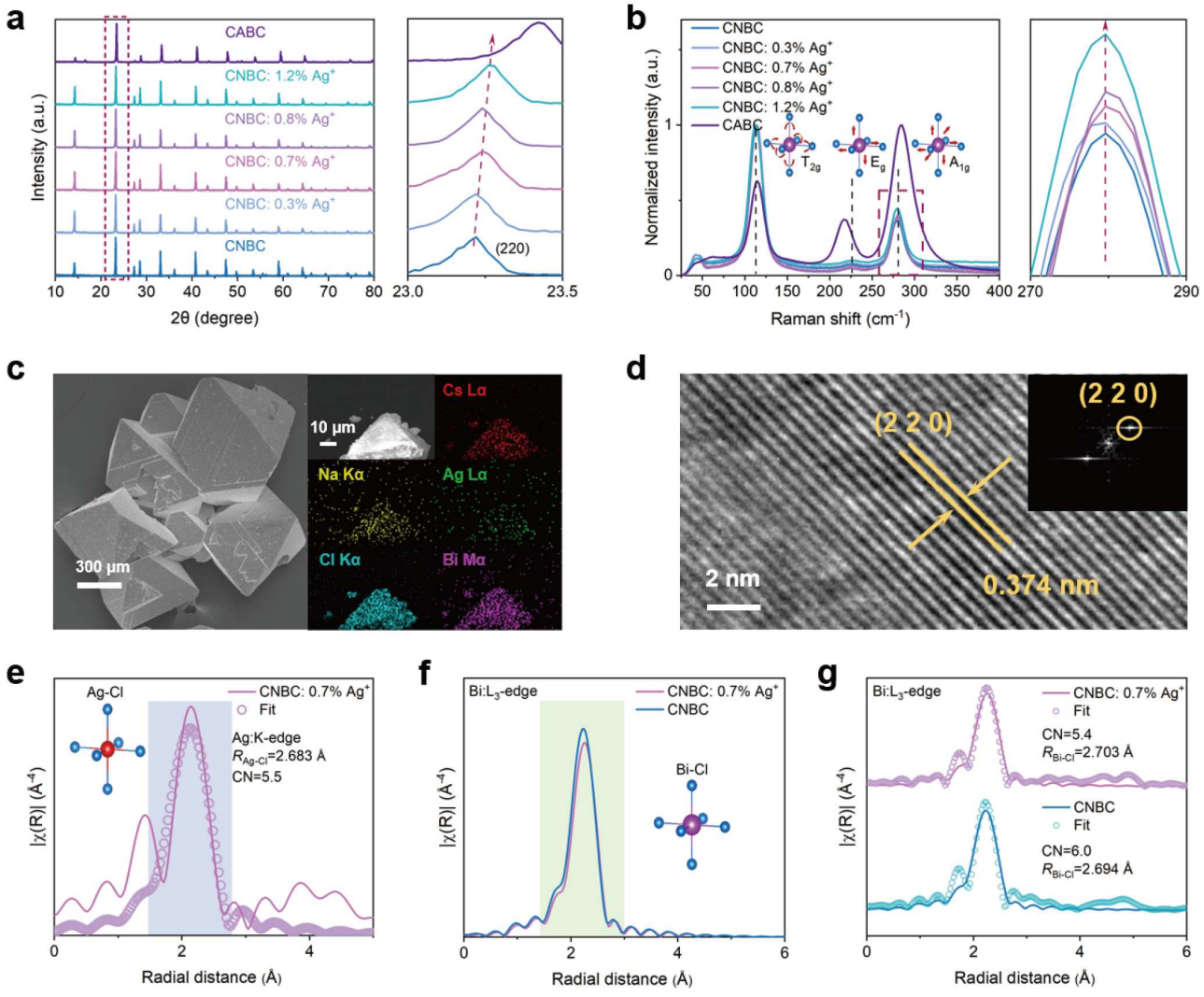

Figure 2 Structural characterization of CNBC: x% Ag^+ DPs. XRD patterns (a) and Raman spectra collected at 532-nm laser irradiation (b) of CABC and CNBC: x% Ag^+ ($0 \leqslant x \leqslant 100$). The enlarged peaks of (220) in the right panel of (a) indicate their shifts towards the larger-angle region with the increased Ag^+ concentration. The schematic diagrams of intrinsic lattice vibrations correspond to each Raman active mode, and the amplified A_{1g} peak in the right panel of (b) rises with increasing Ag^+ concentration. The purple and blue balls indicate Bi^{3+} and Cl^-, respectively. (c) SEM (left) and EDS elemental mapping images (right) of CNBC: 0.7% Ag^+. (d) High-resolution TEM image of CNBC: 0.7% Ag^+. The inset shows the Fast Fourier transform corresponding to the (220) crystal spacing. (e) The measured and EXAFS with fitting curves of the Ag K-edge in R-space of CNBC: 0.7% Ag^+. The EXAFS curves (f) and fitting curves (g) of the Bi L_3-edge in R-space of CNBC: 0.7% Ag^+ and CNBC reference sample.

laser excitation, the samples exhibit three strong Raman modes corresponding to breathing vibrations (T_{2g}: 113 cm^{-1}), asymmetric stretching (E_g:216 cm^{-1}), and symmetric stretching (A_{1g}: 284 cm^{-1}) of the Cl atoms (Fig. 2b). The energy of the A_{1g} mode did not change, but the intensity increased because the $[AgCl_6]^{5-}$ octahedron dominated the $[NaCl_6]^{5-}$ octahedron due to covalency modulation [25]. The peak position of CNBC in the spectrum is more low frequency compared to CABC. Since the frequency is directly proportional to the bond strength, it is expected that longer bonds result in lower energy for the optical phonons, indicating a softer lattice [26,27].

Scanning electron microscopy (SEM) showed that the synthesized CNBC: 0.7% Ag^+ DPs has a typical octahedral morphology (Fig. 2c). The elemental mapping images show a uniform distribution of Cs, Na, Ag, Cl, and Bi through the whole particle. The spacing (0.374 nm) of the (220) plane confirmed by the high-resolution transmission electron microscopy (TEM) image is smaller than the standard spacing (0.383 nm), which was an evidence of lattice shrinkage due to enhanced covalency (Fig. 2d). Moreover, X-ray photoelectron spectroscopy (XPS) confirmed that all elements in the sample exist in the expected oxidation state (Supplementary Information, Fig. S3). The binding energies of Cs, Na, Bi, and Cl in CNBC: 0.7% Ag^+ have little changes compared to CNBC, and the appearance of the weak Ag 3*d* characteristic peak implies that only a trace amount of Ag was doped for substituting Na to form the $[AgCl_6]^{5-}$ octahedron [28,29].

To better illustrate the effect of Ag–Cl covalency on the structure of $[BiCl_6]^{3-}$ octahedra, the XAFS was employed [30]. First, the chemical states of Ag and Bi sites in DPs were characterized by Ag K-edge and Bi L_3-edge X-ray absorption near-edge structure (XAENS) spectra (Supplementary Information, Fig. S4). The extended X-ray absorption fine structure (EXAFS) data as well as fitting results were also shown, where the main peaks in Fig. 2e–g are attributed to scattering interactions between Ag and Cl atoms (Ag–Cl), Bi and Cl atoms (Bi–Cl), respectively. The results of fitting in *R*-space indicate that the six-coordination environment of Ag with an interatomic distance of 2.683 Å was direct evidence that Ag occupies the Na site. Meanwhile, the effect of covalency modulation has a negligible effect on the first shell coordination number of the Bi^{3+} ions. The valence states of Bi were unchanged before and after covalency modulation. In particular, the chemical states of Bi in CNBC and CNBC: 0.7% Ag^+ are very similar. It is revealed that, as the Ag is doped, the coordination number of Bi–Cl decreases slightly from 6.0 to 5.4, which may be caused by Ag–Cl polarization leading to the languishing interaction of Bi–Cl [31,32]. The average Bi–Cl interatomic distance increases from 2.694 to 2.703 Å (Table S2), which agrees with the trend of the first-principles calculations.

Optical properties of trace Ag-doped CNBC: Ag^+

To understand the effect of trace Ag doping on the optical behavior of CNBC DPs, PL spectroscopy experiments were performed, confirming the higher luminescence intensity for the materials after covalency modulation (Fig. 3a). All DPs have a broadband emission in the 400–900 nm range with a full width at half maxima of 246 nm (the shoulder peak at 810 nm is the instrumental noise). And the lattice shrinkage resulting from trace Ag doping did not produce a blueshift in the PL spectra. It shows strong evidence of emission from STEs. The emission peak of CNBC doped with Ag^+ is located at 680 nm in line with CNBC, unlike that at 620 nm for CABC (Supplementary Information, Fig. S5). This indicates that the emission mode of CNBC after Ag^+ doping was unchanged. Notably, CNBC: 0.7% Ag^+ shows the best optical properties with PLQY as high as 89% (Fig. 3b; Supplementary Information, Fig. S6), much higher than the 16% of CNBC. CNBC: 0.7% Ag^+ is promising for near-infrared (NIR) applications due to the broadband emission peaks covering the NIR I band (650–950 nm) [33–36]. Such high PLQY has a great advantage over other perovskite materials in this band region (Fig. 3c, Table S3). CNBC: 0.7% Ag^+ also exhibits excellent environmental stability over a considerable period (Fig. 3d). Notably, our optimized doping concentration

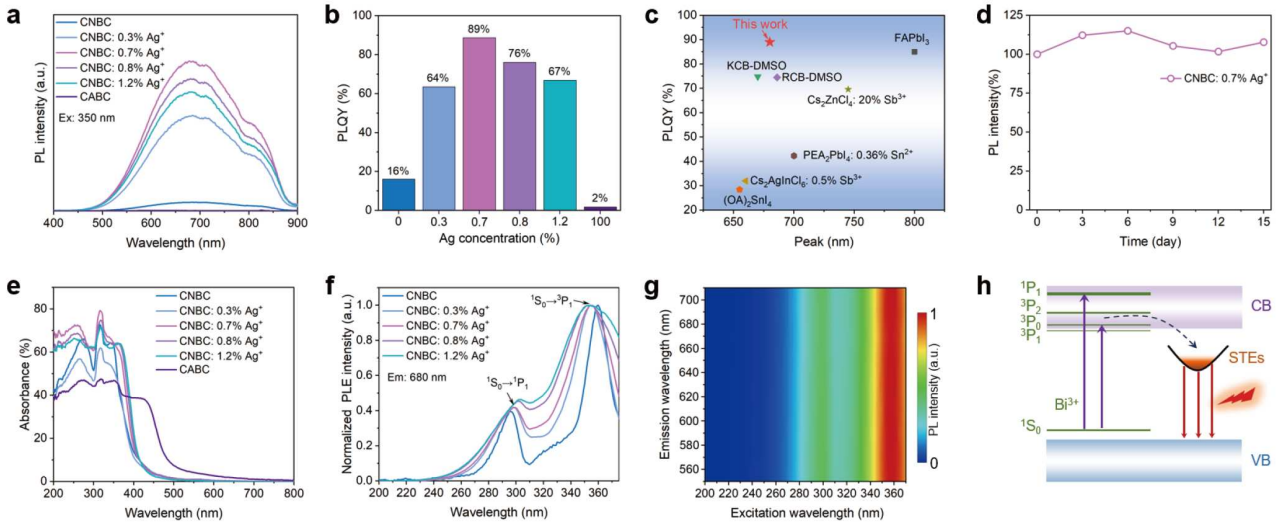

Figure 3 Optical properties of CNBC: *x*% Ag^+ DPs. PL spectra (a) and PLQY (b) of CNBC: *x*% Ag^+ ($0 \leqslant x \leqslant 100$). All measurements were performed at 25 °C. (c) PLQY versus wavelength for various NIR materials. The data are also shown in Table S3. (d) PL intensity of CNBC: 0.7% Ag^+ after being exposed to air for 15 days under ambient conditions. UV/Vis absorption spectra (e), and excitation spectra (f) of CNBC: *x*% Ag^+. (g) Emission intensity versus excitation wavelength for CNBC: 0.7% Ag^+. (h) Simplified energy level scheme for CNBC: 0.7% Ag^+.

demonstrates a significant reduction compared to previously reported counterparts (Table S4).

We further investigated the broadband emission mechanism in DPs. As the Ag^+ concentration increases, the edges of the CNBC: x% Ag^+ ($0 \leqslant x \leqslant 100$) absorption bands red-shift (Fig. 3e), and the Tauc plot shows that the band gaps are gradually decreasing (Supplementary Information, Fig. S7). It is noted that the photoluminescence excitation (PLE) spectrum of CNBC: 0.7% Ag^+ at 680 nm presents a strong and broad excitation band in the 200–375 nm range (Fig. 3f), mostly consisting of two excitation peaks at 300 and 350 nm. This corresponds to the dipole-allowed transition of $^1S_0 \rightarrow {}^1P_1$ and the spin-orbit allowed transition of $^1S_0 \rightarrow {}^3P_1$ for Bi^{3+}. Not only that, the STEs origin of the broadband emission could be experimentally confirmed by the fact that the PLE spectra show the same shapes and features for the emission from 460 to 700 nm as well as the PL spectra for the excitation from 280 to 350 nm, suggesting that the broadband emission originates from the relaxation of the same excited state (Fig. 3g; Supplementary Information, Fig. S8). Based on the above analysis, the NIR emission mechanism in CNBC: 0.7% Ag^+ is proposed (Fig. 3h). When the excitation source irradiates the material, the excitation energy is firstly absorbed by Bi^{3+} ions. Due to the improved optical absorption after covalency modulation, dipole-allowed transitions are enhanced. This leads to an enhanced STE density and the broadband NIR emission after radiative recombination of the STEs.

Trace Ag doping-induced symmetry breaking for promoting carrier generation

The trace Ag doping yields a marked symmetry breaking, leading to an improvement in carrier generation, as directly confirmed by ultrafast femtosecond transient absorption (Fs-TA) spectroscopy. We explored ultrafast photophysical processes during photoexcitation of CNBC and CNBC: 0.7% Ag^+ with a 310 nm femtosecond pulsed laser under the same conditions. In the contour plots of Fs-TA spectra, all samples exhibit similar positive photoinduced absorption (PIA) (Fig. 4a, b; Supplementary Information, Fig. S9), indicating evidence for the formation of STEs in the crystal lattice. In addition, the increased intensity of the PIA signal for CNBC: 0.7% Ag^+ suggests the existence of a dark-state exciton transition to bright-state processes (where undoped CNBC corresponds to dark STEs and CNBC: 0.7% Ag^+ corresponds to bright STEs) [37], in reflection of the improvement in optical absorption. Further kinetic traces show that the rise time of PIA in the probe region from 450–700 nm was about 100 fs shorter than before symmetry breaking (Fig. 4c, Table S5). This means a shorter time for CNBC: 0.7% Ag^+ to reach the STEs state from the ground state (Fig. 4d).

To reveal the phenomenon of faster STE formation in TA spectra, we further investigated the photophysical mechanism by variable-temperature PL spectroscopy. CNBC and CNBC: 0.7% Ag^+ show similar emission properties (Fig. 4e, f; Supplementary Information, Fig. S10), and the PL intensity decreases continuously with increasing temperature, which could be explained by the emergence of thermally activated nonradiative recombination processes [38]. At the same time, the PL peak position experiences a monotonic blueshift, suggesting that temperature-induced thermal expansion of the lattice rather than electron-phonon coupling dominates the evolution of the photoluminescence emission energy [39,40]. By fitting the temperature-dependent PL intensity with the Arrhenius equation, the exciton binding energy (E_b) of CNBC: 0.7% Ag^+ was calculated to be about 150.8 meV (Fig. 4g), significantly lower than that of CNBC (274.5 meV). During the formation of STEs, the low binding energy favors the dissociation of excitons to form carriers, which could be trapped by the lattice distortion after symmetry breaking, thus favoring the formation of STEs states (Fig. 4h).

Trace Ag-doping induced vacancy suppression for enhanced STEs emission

It is proven that the poor PL properties of DPs also stem from the formation of chlorine vacancies during the phase of crys-

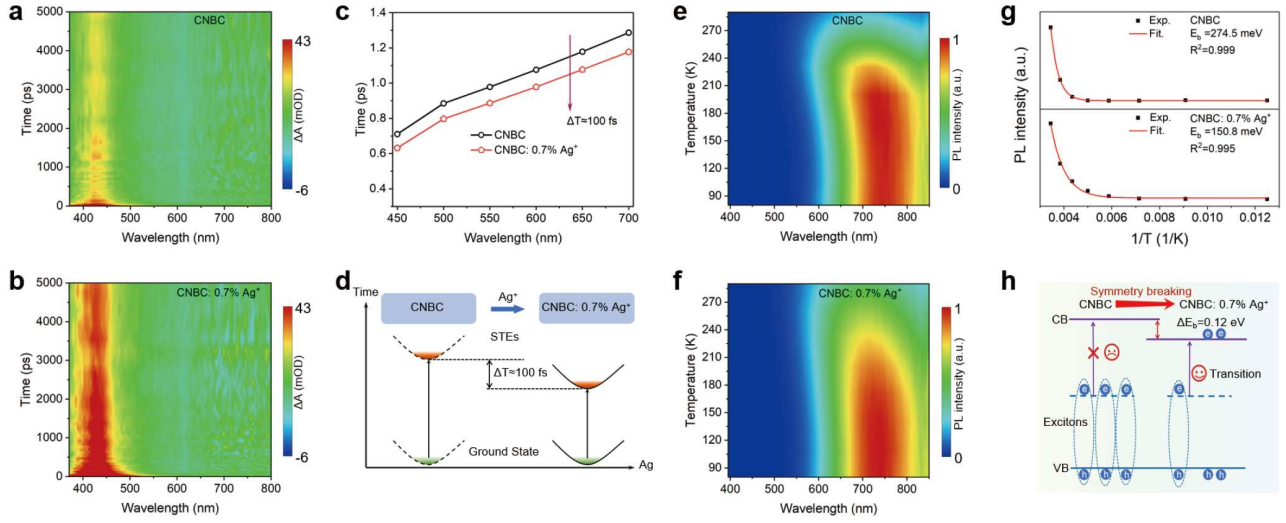

Figure 4 Symmetry breaking *via* trace Ag doping for promoting carrier generation. Transient absorption spectra for CNBC (a) and CNBC: 0.7% Ag^+ (b) (laser pulse of 310 nm and 0.6 mW). (c) The rise time of the PIA kinetic curves in the probe region from 450 to 700 nm. (d) Schematic diagram from the ground state to the STEs state for CNBC and CNBC: 0.7% Ag^+. Contour plots of the temperature-dependent PL emission spectra for CNBC (e) and CNBC: 0.7% Ag^+ (f). (g) Integrated PL intensity of STEs for CNBC and CNBC: 0.7% Ag^+. (h) Schematic diagram of local symmetry breaking affecting the excitons production and electron transition.

tallization [41,42]. As shown in Fig. 5a, in the hydrochloric acid environment, the Na–Cl bond is strongly ionic, causing Na^+ and Cl^- to form two isolated ionic portions in the solvent [43]. The covalent interaction of trace Ag^+ and Cl^- can inhibit the generation of chlorine vacancy defects during the nucleation of DPs. We then performed the electron paramagnetic resonance spectroscopy (EPR) measurements (Fig. 5b). Both CNBC and CNBC: 0.7% Ag^+ show a Lorentzian line with $g\approx2.01$, evidencing a typical character of free electrons [44]. This is caused by the unpaired free electrons provided by the chlorine vacancies. The decreased signal intensity reveals that covalency modulation suppresses the chlorine vacancy defect density.

Here, to verify that chlorine vacancies are the non-radiative recombination center, a batch of CNBC: 0.7% Ag^+ samples was synthesized in different concentrations of hydrochloric acid. The XRD patterns of this batch all show a pure phase structure (Supplementary Information, Fig. S11a), and the diffraction angle shifts to a high angle with decreasing hydrochloric acid concentration. This is a sign of lattice shrinkage due to the increased chlorine vacancy density. In addition, the EPR spectra exhibit that the lower hydrochloric acid concentration could lead to a higher chlorine vacancy density (Fig. 5c), and this is in concordance with the XRD results. The increased chlorine vacancy density led to a decrease in the PL intensity (Fig. 5d; Supplementary Information, Fig. S11b), proving that chlorine vacancies are the non-radiative recombination center. In summary, we have shown that covalency modulation can suppress the formation of chlorine vacancy defects and reduce the non-radiative recombination.

There is evidence for the suppression of chlorine vacancies by covalency modulation in the formation kinetics of STEs as well. The PIA decay signal (425 nm) of DPs in Fs-TA spectra could be fitted by three components: the ultrafast lifetime of τ_1, the middle lifetime of τ_2, and the slow lifetime of τ_3, attributed to the formation time of the STEs state, the time of intra-band relaxation, and radiative recombination induced by the STEs state, respectively (Fig. 5e, f). In particular, the ultrafast component (τ_1) and the middle component (τ_2) were assigned to volume defects trapping and surface trap trapping, respectively [45,46]. The time-resolved photoluminescence decay lifetime (TRPL) measurements showed that the fluorescence lifetime was extended (from 7.94 to 8.21 μs) after covalency modulation (Fig. 5g; Supplementary Information, Fig. S12), which was in agreement with the increasing of τ_3 lifetime. This was proof of the enhancement of radiative recombination [47]. We fitted the fluorescence lifetime decay curves to obtain a short-lived component (2.7 μs for CNBC; 7.0 μs for CNBC: 0.7% Ag^+) and a long-lived component (8.3 μs for CNBC; 17.2 μs for CNBC: 0.7% Ag^+). This is also a result of chlorine vacancy suppression. In general, covalency resulting from Ag–Cl bonds suppresses chlorine vacancy formation during CNBC: 0.7% Ag^+ nucleation. Thus, the radiative recombination replaces the non-radiative recombination in CNBC: 0.7% Ag^+, and the higher STEs density is responsible for stronger broadband emission (Fig. 5h).

NIR LED assembly based on CNBC: 0.7% Ag^+

CNBC: 0.7% Ag^+ has ultra-high stability in air (Supplementary Information, Fig. S13), with ultra-broad emission covering the NIR region as well as ultra-high PLQY. To further prove its practical application, we fabricated an NIR LED by combining the CNBC: 0.7% Ag^+ phosphor with a commercial 365 nm UV-LED chip (Fig. 6a). The NIR LED device based on CNBC: 0.7% Ag^+ DPs has strong NIR emission under the 650 nm filter (Fig. 6b). It displays ultra-broad emission from 400 to 1000 nm with a peak at 689 nm with a chromaticity coordinate of (0.536, 0.431) (Fig. 6c, d). The NIR LED possesses a good color rendering index (Ra=89) (Supplementary Information, Fig. S14) and excellent optoelectronic performance, with a good linear relationship between emission intensity and excitation power (Fig. 6e, f).

We demonstrated the promise of NIR LED device in the field of nondestructive analysis by measuring the absorption spectra of several substances, such as watermelon, apple, tomato, and blueberry. We first built a testing light path by using the fabricated NIR LED as a light source (Fig. 6g). The fruits in the area to be tested absorbed the broadband emission from the NIR

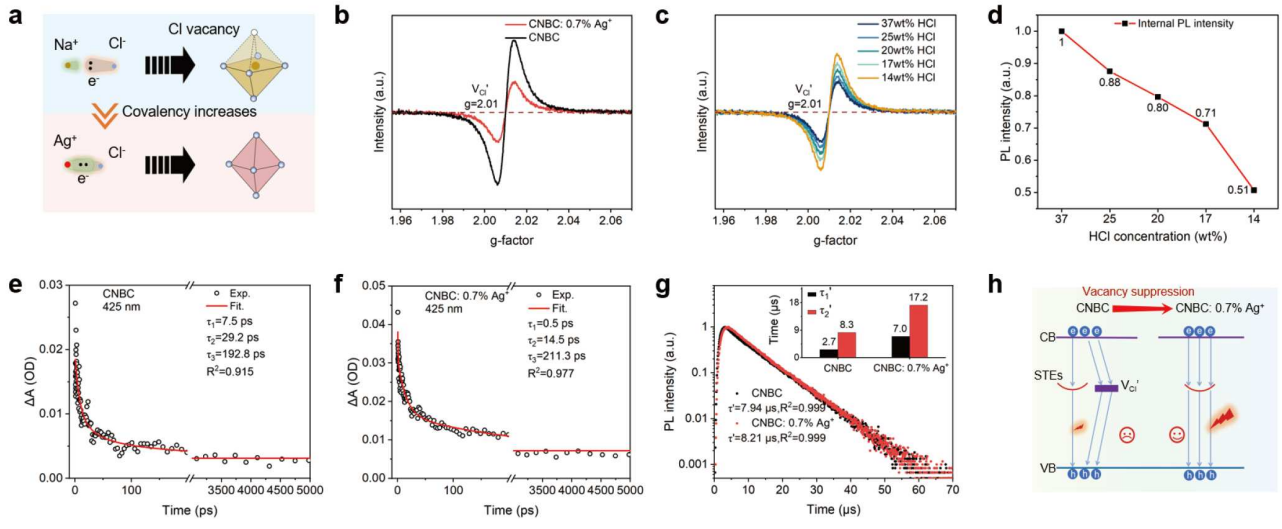

Figure 5 Vacancy suppression *via* trace Ag doping for improved STEs emission. (a) Schematic diagram of vacancy suppression during nucleation. (b) EPR of CNBC and CNBC: 0.7% Ag^+. EPR (c) and PL intensity (d) of CNBC: 0.7% Ag^+ synthesized at different concentrations of hydrochloric acid. PIA decay dynamics of CNBC (e) and CNBC: 0.7% Ag^+ (f) probed at 425 nm. (g) TR-PL decay curves. (h) Schematic diagram of vacancy suppression for enhancing STEs.

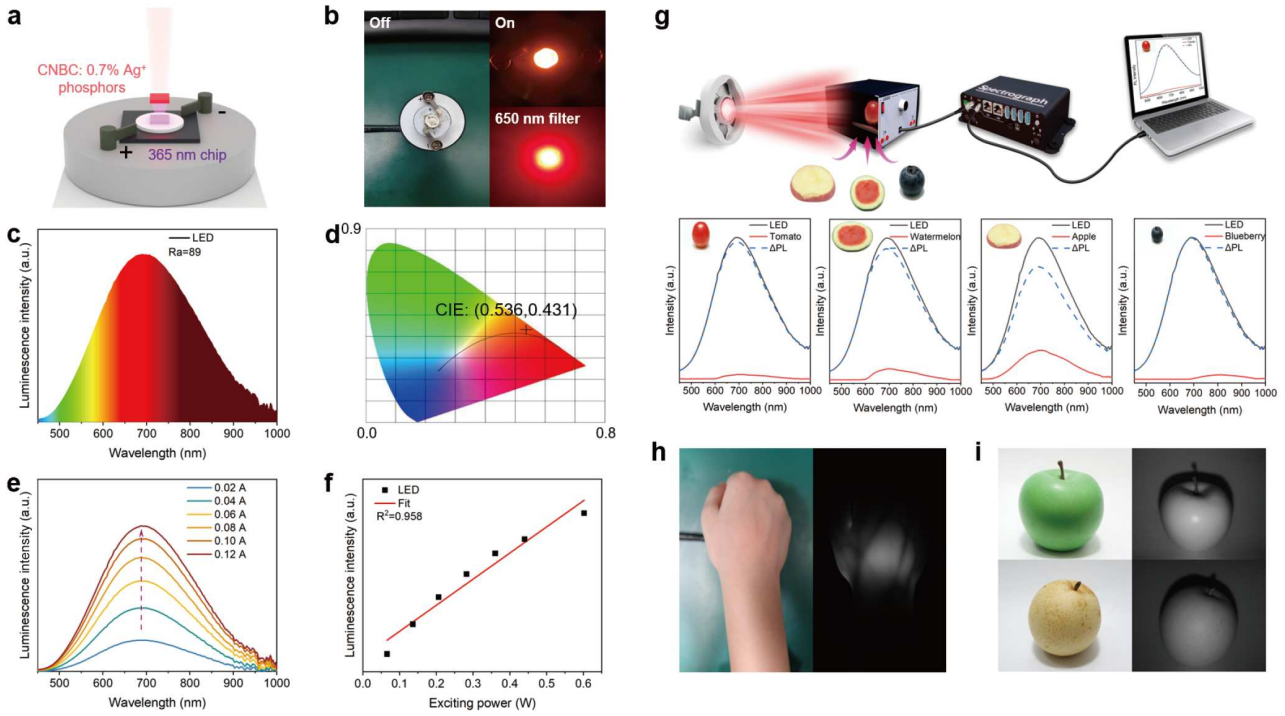

Figure 6 Application demonstration of NIR LED with CNBC: 0.7% Ag^+. The model of the NIR LED (a) and photos of the light emitted under power (b). Red light is emitted under a 650 nm filter. Emission spectrum (c), CIE chromaticity diagram (d) of NIR LED. Luminescence spectra (e) and dependence (f) of the Vis-NIR-emitting intensity of NIR LED on the operating current from 20 to 120 mA. (g) Schematic diagram of the experimental setup for measuring absorption (top panel), and fingerprint spectra of different fruits (down panel). (h) Photos of the fist after transillumination of NIR light. (i) Photographs of apple and pear under daylight and upon illumination with NIR LED.

LED, and the fiber-optic spectrometer received the penetrated signal and output it to a computer. In the test, it was found that the color and thickness of the fruits would generate the corresponding fingerprint spectra. The colors of the fruits correspond to the signal start points (600 nm for tomato, 700 nm for blueberry), and the species of the fruits determine the absorption capacity (watermelon absorbs more than apple) at the same thickness. This may be due to the fruit colors and photosensitive pigments related to the absorption. And it could be used in the field of rapid fruit screening (e.g., tomato has different colors at different stages of ripening). In addition, medical imaging could be achieved through the absorption of NIR emission by chromophores in blood (Fig. 6h; Supplementary Information, Fig. S15a). When the NIR light illuminates the fist, the venous blood vessels on the back of the hand are recognized by the NIR camera, and a black-and-white image is recorded. Finally, we also demonstrated the application of NIR LED in night vision (Fig. 6i; Supplementary Information, Fig. S15b). After being turned on, the NIR camera could clearly capture the contours and the shadows of the fruits, which were displayed in black and white.

CONCLUSIONS

In summary, the trace Ag-triggered covalency modulation strategy has been developed to effectively improve the luminescence efficiency of the CNBC. Experimental and theoretical calculations confirm the enhanced covalency of CNBC DPs by introducing trace Ag^+. It could lead to significant local symmetry breaking and Cl vacancy suppressing, thus effectively lowering exciton binding energy by 0.12 eV and enhancing the STEs density. It is notable that the as-prepared CNBC: 0.7% Ag^+ shows a high PLQY of 89%, 5.6 times that of pure CNBC in the NIR-I region and much superior to those reported NIR emitting materials. It also demonstrates excellent structural and PL stability under ambient conditions. Finally, this material could be combined with a 365 nm UV-LED chip for successful demonstration in nondestructive spectral analysis and night vision illumination. This study provides a promising strategy of trace metal doping for photoluminescent emitters with high-efficiency emission.

Received 10 April 2025; accepted 3 June 2025; published online 7 July 2025

1 Wang L, Xie RJ, Suehiro T, *et al.* Down-conversion nitride materials for solid state lighting: recent advances and perspectives. Chem Rev, 2018, 118: 1951–2009
2 Tan ZK, Moghaddam RS, Lai ML, *et al.* Bright light-emitting diodes based on organometal halide perovskite. Nat Nanotech, 2014, 9: 687–692
3 Rajendran V, Fang MH, Guzman GND, *et al.* Super broadband near-infrared phosphors with high radiant flux as future light sources for spectroscopy applications. ACS Energy Lett, 2018, 3: 2679–2684
4 Qiao J, Zhou G, Zhou Y, *et al.* Divalent europium-doped near-infrared-emitting phosphor for light-emitting diodes. Nat Commun, 2019, 10: 5267
5 Li S, Luo J, Liu J, *et al.* Self-trapped excitons in all-inorganic halide perovskites: fundamentals, status, and potential applications. J Phys Chem Lett, 2019, 10: 1999–2007
6 Zeng R, Zhang L, Xue Y, *et al.* Highly efficient blue emission from self-trapped excitons in stable Sb^{3+}-doped $Cs_2NaInCl_6$ double perovskites. J Phys Chem Lett, 2020, 11: 2053–2061
7 Jiang F, Wu Z, Lu M, *et al.* Broadband emission origin in metal halide perovskites: Are self-trapped excitons or ions? Adv Mater, 2023, 35:

2211088
8 Pu G, Wang R, Tang Y, *et al.* Cation doping engineering of metal halide perovskites for high-energy X-ray exploration. Mater Chem Front, 2025, 9: 1954–1970
9 Arfin H, Kshirsagar AS, Kaur J, *et al.* ns^2 electron (Bi^{3+} and Sb^{3+}) doping in lead-free metal halide perovskite derivatives. Chem Mater, 2020, 32: 10255–10267
10 Su B, Li M, Song E, *et al.* Sb^{3+}-doping in cesium zinc halides single crystals enabling high-efficiency near-infrared emission. Adv Funct Mater, 2021, 31: 2105316
11 Lin L, Jones TW, Yang TCJ, *et al.* Hydrogen bonding in perovskite solar cells. Matter, 2024, 7: 38–58
12 Luo J, Wang X, Li S, *et al.* Efficient and stable emission of warm-white light from lead-free halide double perovskites. Nature, 2018, 563: 541–545
13 Zhang G, Wang D, Lou B, *et al.* Efficient broadband near-infrared emission from lead-free halide double perovskite single crystal. Angew Chem Int Ed, 2022, 61: e202207454
14 Zhu D, Zito J, Pinchetti V, *et al.* Compositional tuning of carrier dynamics in $Cs_2Na_{1-x}Ag_xBiCl_6$ double-perovskite nanocrystals. ACS Energy Lett, 2020, 5: 1840–1847
15 Yang B, Mao X, Hong F, *et al.* Lead-free direct band gap double-perovskite nanocrystals with bright dual-color emission. J Am Chem Soc, 2018, 140: 17001–17006
16 Pei Y, Tu D, Li C, *et al.* Boosting near-infrared luminescence of lanthanide in $Cs_2AgBiCl_6$ double perovskites via breakdown of the local site symmetry. Angew Chem Int Ed, 2022, 61: e202205276
17 Ravel B, Newville M. *ATHENA*, *ARTEMIS*, *HEPHAESTUS*: data analysis for X-ray absorption spectroscopy using *IFEFFIT*. J Synchrotron Rad, 2005, 12: 537–541
18 Abdi-Jalebi M, Pazoki M, Philippe B, *et al.* Dedoping of lead halide perovskites incorporating monovalent cations. ACS Nano, 2018, 12: 7301–7311
19 Zheng W, Sun R, Liu Y, *et al.* Excitation management of lead-free perovskite nanocrystals through doping. ACS Appl Mater Interfaces, 2021, 13: 6404–6410
20 Liu Z, Sun Y, Cai T, *et al.* Two-dimensional $Cs_2AgIn_xBi_{1-x}Cl_6$ alloyed double perovskite nanoplatelets for solution-processed light-emitting diodes. Adv Mater, 2023, 35: 2211235
21 Kim YH, Kim S, Kakekhani A, *et al.* Comprehensive defect suppression in perovskite nanocrystals for high-efficiency light-emitting diodes. Nat Photonics, 2021, 15: 148–155
22 Zhang X, Song JN, Sun TM, *et al.* Constructing nanoneedle arrays of heterostructured RuO_2-Co_3O_4 with tip-effect-induced enrichment of reactants for enhanced water oxidation. Chem Commun, 2025, doi:10.1039/d1035cc01933h
23 Feng Y, Wang X, Ma J, *et al.* A solid-solution with asymmetric Ni-O-Cr sites for boosting protonation toward anodic oxidation. Adv Energy Mater, 2024, 14: 2401501
24 Zhu H, Wang JJ, Xu Z, *et al.* Pd nanoparticle size-dependent H^* coverage for Cu-catalyzed nitrate electro-reduction to ammonia in neutral electrolyte. Small, 2024, 20: 2404919
25 Cheng X, Xie Z, Zheng W, *et al.* Boosting the self-trapped exciton emission in alloyed Cs_2(Ag/Na)$InCl_6$ double perovskite via Cu^+ doping. Adv Sci, 2022, 9: 2103724
26 Li X, Fu Y, Pedesseau L, *et al.* Negative pressure engineering with large cage cations in 2D halide perovskites causes lattice softening. J Am Chem Soc, 2020, 142: 11486–11496
27 Miyata K, Atallah TL, Zhu XY. Lead halide perovskites: crystal-liquid duality, phonon glass electron crystals, and large polaron formation. Sci Adv, 2017, 3: e1701469
28 Wang M, Tang Y, Deng M, *et al.* $Cs_2Ag_{0.1}Na_{0.9}BiCl_6$:$Tm^{3+}$ double perovskite: coprecipitation preparation and near-infrared emission. J InOrg Mater, 2023, 38: 1083–1088
29 Feng Y, Ran N, Wang X, *et al.* Nanoparticulate WN/Ni_3C coupling in ceramic coatings for boosted urea electro-oxidation. Adv Energy Mater, 2023, 13: 2302452
30 Wang J, He W, Zong Y, *et al.* Electronic redistribution induced by interaction between ruthenium nanoparticles and Ni-N(O)-C sites boosts alkaline water electrolysis. Chem Commun, 2024, 60: 9444–9447
31 Weng Z, Liu L, Hu Y, *et al.* Significance of engineering the MnO_6 octahedral units to promote the oxygen reduction reaction of perovskite oxides. Adv Mater, 2023, 36: 2311102
32 Qin Y, Yu T, Deng S, *et al.* RuO_2 electronic structure and lattice strain dual engineering for enhanced acidic oxygen evolution reaction performance. Nat Commun, 2022, 13: 3784
33 Vasilopoulou M, Fakharuddin A, García de Arquer FP, *et al.* Advances in solution-processed near-infrared light-emitting diodes. Nat Photon, 2021, 15: 656–669
34 Pu G, Song J, Cheng Z, *et al.* Interfacial molecular engineering of rare earth-doped nanocrystals: basic principles, construction strategies, and advanced applications. Laser Photonics Rev, 2025, 19: 2500156
35 Zhang A, Liu Y, Liu G, *et al.* Dopant and compositional modulation triggered broadband and tunable near-infrared emission in $Cs_2Ag_{1-x}Na_xInCl_6$:Cr^{3+} nanocrystals. Chem Mater, 2022, 34: 3006–3012
36 Liu G, Chen W, Xiong Z, *et al.* Laser-driven broadband near-infrared light source with watt-level output. Nat Photon, 2024, 18: 562–568
37 Han P, Mao X, Yang S, *et al.* Lead-free sodium-indium double perovskite nanocrystals through doping silver cations for bright yellow emission. Angew Chem Int Ed, 2019, 58: 17231–17235
38 Ma Z, Shi Z, Qin CC, *et al.* Stable yellow light-emitting devices based on ternary copper halides with broadband emissive self-trapped excitons. ACS Nano, 2020, 14: 4475–4486
39 Zhang D, Eaton SW, Yu Y, *et al.* Solution-phase synthesis of cesium lead halide perovskite nanowires. J Am Chem Soc, 2015, 137: 9230–9233
40 Zhang J, Yang Y, Deng H, *et al.* High quantum yield blue emission from lead-free inorganic antimony halide perovskite colloidal quantum dots. ACS Nano, 2017, 11: 9294–9302
41 Wu T, Li J, Zou Y, *et al.* High-performance perovskite light-emitting diode with enhanced operational stability using lithium halide passivation. Angew Chem Int Ed, 2020, 59: 4099–4105
42 Shen X, Kang K, Yu Z, *et al.* Passivation strategies for mitigating defect challenges in halide perovskite light-emitting diodes. Joule, 2023, 7: 272–308
43 Sun Y, Liao H, Wang J, *et al.* Covalency competition dominates the water oxidation structure-activity relationship on spinel oxides. Nat Catal, 2020, 3: 554–563
44 Pi J, Jia X, Long Z, *et al.* Surface and defect engineering coupling of halide double perovskite $Cs_2NaBiCl_6$ for efficient CO_2 photoreduction. Adv Energy Mater, 2022, 12: 2202074
45 Yang B, Hong F, Chen J, *et al.* Colloidal synthesis and charge-carrier dynamics of $Cs_2AgSb_{1-y}Bi_yX_6$ (X: Br, Cl $0 \leqslant y \leqslant 1$) double perovskite nanocrystals. Angew Chem Int Ed, 2019, 58: 2278–2283
46 Zhu J, Park S, Gong OY, *et al.* Formamidine disulfide oxidant as a localised electron scavenger for >20% perovskite solar cell modules. Energy Environ Sci, 2021, 14: 4903–4914
47 Chen Y, Wang Z, Wei Y, *et al.* Exciton localization for highly luminescent two-dimensional tin-based hybrid perovskites through tin vacancy tuning. Angew Chem Int Ed, 2023, 62: e202301684

Acknowledgement This work was supported by the National Natural Science Foundation of China (92163117, 52072389). Wang J thanks the Central Guidance on Science and Technology Development Fund of Zhejiang Province (2024ZY01011) for financial support.

Author contributions Wang M designed and engineered the samples; Tang M and Zhou Z performed the DFT simulation; Wang Z and Liu L performed the EXAFS experiment; Li J performed the Fs-TA experiment; Wang M wrote the paper with support from Pu G, Tang M, Kang C, Chen W, Wang D and Wang J; All authors contributed to the general discussion.

Conflict of interest The authors declare that they have no conflict of interest.

Supplementary information Supplementary materials are available in the online version of the paper.

Machao Wang is now a PhD candidate at the Shanghai Institute of Ceramics, Chinese Academy of Sciences (SICCAS) under the supervision of Prof. Jiacheng Wang and Prof. Dong Wang. His current research focuses on luminescent materials.

Dong Wang is a full professor at SICCAS. He obtained his PhD degree from Zhejiang University in 1999. His current research focuses on scintillator crystals and highly efficient luminescent materials.

Jiacheng Wang is currently a full professor of materials science at Taizhou University and Head of Zhejiang Key Laboratory of Island Green Energy and New Materials. He obtained his PhD degree from SICCAS in 2007. Before getting back to SICCAS in 2013, he spent 6 years on functional materials research at the University of Tokyo (Collaborator: Prof. Makoto Onaka), Dresden University of Technology (Collaborator: Prof. Stefan Kaskel), and Cardiff University (Collaborator: Prof. Graham Hutchings). From 2013 to 2023, he was a professor at SICCAS. His present research focuses on rational design and preparation of advanced functional materials for energy transformation and photoluminescence.

微量银掺杂增强金属卤化物钙钛矿的光致发光量子产率

王马超[1,2†], 唐扬敏[1,2†], 蒲贵强[3], 康成彬[4], 王志强[5], 刘俪佳[5], 李敬[6], 周真真[1], 陈伟[7], 王东[1,2*], 王家成[1,3*]

摘要 自陷激子普遍存在于具有软晶格和强激子-声子耦合特性的金属卤化物钙钛矿(MHPs)中, 具有宽带发射和大斯托克斯位移的发光特点, 特别适用于发光二极管. 然而, MHPs的光致发光量子产率(PLQY)同时受到高的激子结合能和与卤素空位相关的非辐射复合的限制. 本文中, 我们通过在$Cs_2NaBiCl_6$双钙钛矿中掺杂微量银(Ag), 将PLQY从16%大幅提升至89%, 该性能优于此前报道的所有基于$Cs_2NaBiCl_6$的发光体. 实验和理论研究结果揭示了微量Ag掺杂引发的共价相互作用导致材料局部对称性破缺, 从而使激子结合能降低0.12 eV, 进而改善光激发过程. 同时, 这种共价相互作用能够钝化氯空位缺陷, 有效抑制了非辐射复合. 因此, $Cs_2NaBiCl_6$: 0.7% Ag^+能够积聚大量自陷激子, 大幅提高了PLQY值. 最后, 我们利用$Cs_2NaBiCl_6$: 0.7% Ag^+组装了近红外发光二极管, 表明了其在无损光谱分析和夜视照明领域的应用前景. 本工作展示了一种可以提升用于先进光电器件的MHPs光发射性能的有效策略.